

# Polarization-independent amplification and frequency conversion in strongly-birefringent fibers

C. J. McKinstry and C. Xie

*Bell Laboratories, Alcatel-Lucent, Holmdel, New Jersey 07733*

[mckinstry@alcatel-lucent.com](mailto:mckinstry@alcatel-lucent.com)

**Abstract:** The inverse modulation interaction is a degenerate four-wave mixing process in which two strong pumps drive a weak signal, whose frequency is the average of the pump frequencies. Theoretical analyses and numerical simulations of this process are made for wave frequencies that are near the zero-dispersion frequency of a fiber, in which case dispersion is unimportant, and wave frequencies that are far from the zero-dispersion frequency, in which case dispersion is important. The results show that the inverse modulation interaction in a strongly-birefringent fiber amplifies a linearly-polarized signal by an amount that depends on its phase angle, but not its polarization angle. Phase conjugation and Bragg scattering are nondegenerate four-wave mixing processes in which two strong pumps drive a weak signal and a weak idler. Studies show that phase conjugation and Bragg scattering in strongly-birefringent fibers produce polarization-independent phase-insensitive amplification and frequency conversion, respectively.

© 2008 Optical Society of America

**OCIS codes:** (060.2320) fiber optics, amplifiers and oscillators; (190.4380) nonlinear optics, four-wave mixing.

---

## References and links

1. J. Hansryd, P. A. Andrekson, M. Westlund, J. Li and P. O. Hedekvist, "Fiber-based optical parametric amplifiers and their applications," *J. Sel. Top. Quantum Electron.* **8**, 506–520 (2002).
2. S. Radic and C. J. McKinstry, "Two-pump fiber parametric amplifiers," *Opt. Fiber Technol.* **9**, 7–23 (2003).
3. C. J. McKinstry, S. Radic and A. H. Gnauck, "All-optical signal processing by fiber-based parametric devices," *Opt. Photon. News* **18** (3), 34–40 (2007).
4. C. J. McKinstry, S. Radic and C. Xie, "Parametric instabilities driven by orthogonal pump waves in birefringent fibers," *Opt. Express* **11**, 2619–2633 (2003).
5. C. J. McKinstry, H. Kogelnik, R. M. Jopson, S. Radic and A. V. Kanaev, "Four-wave mixing in fibers with random birefringence," *Opt. Express* **12**, 2033–2055 (2004).
6. C. J. McKinstry, H. Kogelnik and L. Schenato, "Four-wave mixing in a rapidly-spun fiber," *Opt. Express* **14**, 8516–8534 (2006).
7. T. Hasegawa, K. Inoue and K. Oda, "Polarization independent frequency conversion by fiber four-wave mixing with a polarization diversity technique," *IEEE Photon. Technol. Lett.* **5**, 947–949 (1993).
8. K. K. Chow, C. Shu, C. Lin and A. Bjarklev, "Polarization-insensitive widely tunable wavelength converter based on four-wave mixing in a dispersion-flattened nonlinear photonic crystal fiber," *IEEE Photon. Technol. Lett.* **17**, 624–626 (2005).
9. Z. Wang, N. Deng, C. Lin and C. K. Chan, "Polarization-insensitive widely tunable wavelength conversion based on four-wave mixing using dispersion-flattened high-nonlinearity photonic crystal fiber with residual birefringence," *ECOC 2006*, paper We3.P.18.

10. A. S. Lenihan and G. M. Carter, "Polarization-insensitive wavelength conversion at 40 Gb/s using birefringent nonlinear fiber," CLEO 2007, paper CThAA2.
11. R. H. Stolen, M. A. Bösch and C. Lin, "Phase matching in birefringent fibers," *Opt. Lett.* **6**, 213–215 (1981).
12. C. J. McKinstrie and S. Radic, "Phase-sensitive amplification in a fiber," *Opt. Express* **12**, 4973–4979 (2004).
13. C. J. McKinstrie, R. O. Moore, S. Radic and R. Jiang, "Phase-sensitive amplification of chirped optical pulses in fibers," *Opt. Express* **15**, 3737–3758 (2007).
14. C. J. McKinstrie and M. G. Raymer, "Four-wave-mixing cascades near the zero-dispersion frequency," *Opt. Express* **14**, 9600–9610 (2006).
15. C. J. McKinstrie, S. Radic, M. G. Raymer and L. Schenato, "Unimpaired phase-sensitive amplification by vector four-wave mixing near the zero-dispersion frequency," *Opt. Express* **15**, 2178–2189 (2007).
16. K. Croussore and G. Li, "Phase regeneration of NRZ-DPSK signals based on symmetric-pump phase-sensitive amplification," *IEEE Photon. Technol. Lett.* **19**, 864–866 (2007).
17. C. J. McKinstrie, S. Radic and A. R. Chraplyvy, "Parametric amplifiers driven by two pump waves," *IEEE J. Sel. Top. Quantum Electron.* **8**, 538–547 and 956 (2002).
18. C. R. Menyuk, "Nonlinear pulse propagation in birefringent optical fibers," *IEEE J. Quantum Electron.* **23**, 174–176 (1987).
19. C. J. McKinstrie, H. Kogelnik, G. G. Luther and L. Schenato, "Stokes-space derivations of generalized Schrödinger equations for wave propagation in various fibers," *Opt. Express* **15**, 10964–10983 (2007).
20. G. B. Whitham, *Linear and Nonlinear Waves* (Wiley, 1974).
21. M. Karlsson, "Four-wave mixing in fibers with randomly varying zero-dispersion wavelength," *J. Opt. Soc. Am. B* **15**, 2269–2275 (1998).
22. J. Rothenberg, "Modulational instability for normal dispersion," *Phys. Rev. A* **42**, 682–685 (1990).
23. P. D. Drummond, T. A. B. Kennedy, J. M. Dudley, R. Leonhardt and J. D. Harvey, "Cross-phase modulational instability in high-birefringence fibers," *Opt. Commun.* **78**, 137–142 (1990).
24. C. J. McKinstrie and S. Radic, "Parametric amplifiers driven by two pumps with dissimilar frequencies," *Opt. Lett.* **27**, 1138–1140 (2002).
25. C. J. McKinstrie, J. D. Harvey, S. Radic and M. G. Raymer, "Translation of quantum states by four-wave mixing in fibers," *Opt. Express* **13**, 9131–9142 (2005).
26. C. J. McKinstrie, S. Radic and C. Xie, "Phase conjugation driven by orthogonal pump waves in birefringent fibers," *J. Opt. Soc. Am. B* **20**, 1437–1446 (2003).
27. R. Tang, P. Devgan, P. L. Voss, V. S. Grigoryan and P. Kumar, "In-line frequency-nondegenerate phase-sensitive fibre parametric amplifier for fibre-optic communication," *IEEE Photon. Technol. Lett.* **17**, 1845–1847 (2005).
28. R. Tang, J. Lasri, P. S. Devgan, V. Grigoryan, P. Kumar and M. Vasilyev, "Gain characteristics of a frequency nondegenerate phase-sensitive fiber-optic parametric amplifier with phase self-stabilized input," *Opt. Express* **13**, 10483–10493 (2005).

---

## 1. Introduction

Parametric devices (PDs) based on four-wave mixing (FWM) in fibers can amplify, frequency convert, phase conjugate, regenerate and sample optical signals [1, 2, 3]. However, because transmission fibers do not preserve the signal polarizations, practical PDs must operate in signal-polarization independent manners. The polarization properties of degenerate and non-degenerate FWM, in strongly-birefringent, randomly-birefringent and rapidly-spun fibers were reviewed recently [4, 5, 6]. Most of these processes depend sensitively on the signal polarization. One such polarization-dependent process is the modulation interaction (MI), in which a strong pump amplifies a weak signal and generates a weak idler. The difference between the idler and pump frequencies equals the difference between the pump and signal frequencies.

Devices based on MI (degenerate FWM) can be made polarization independent by the use of polarization-diversity schemes. In one scheme [7, 8], a polarization beam-splitter is used to split the pump and signal into components ( $x$  and  $y$ ), which propagate through a fiber loop in opposite directions. The  $x$ -component of the signal experiences MI driven by the  $x$ -component of the pump, whereas the  $y$ -component of the signal experiences MI driven by the  $y$ -component of the pump. Because the  $x$  and  $y$  components of the waves counterpropagate, the MIs develop independently. If the pump is linearly-polarized at  $45^\circ$  to the axes of the beam splitter (so the pump components have equal powers), the signal components are amplified by the same amount, then recombined by the beam splitter. Hence, the output-signal power does not depend on the input-signal polarization.

In the other scheme [9, 10], the pump and signal propagate through a strongly-birefringent fiber (SBF), in the same direction. If the pump and signal frequencies are similar, the interactions between the  $x$ -component of the pump and  $y$ -component of the signal, and the  $y$ -component of the pump and  $x$ -component of the signal, are suppressed by birefringence [11]. Hence, the MIs of  $x$ -polarized and  $y$ -polarized waves develop independently. If the pump is linearly-polarized at  $45^\circ$  to the birefringence axes, the signal components are amplified by the same amount. Hence, the output-signal power does not depend on the input-signal polarization.

A parametric process is termed phase sensitive if the output-signal power depends on the input-signal phase. Otherwise it is termed phase insensitive. The aforementioned realizations of MI are all phase insensitive. However, there is a degenerate FWM process in which two strong pumps drive a weak signal, whose frequency is the average of the pump frequencies. This process, which is called the inverse MI, is phase sensitive [12, 13]. At present, there is considerable interest in phase-sensitive processes, because of their ability to amplify signals without adding excess noise, and remove phase noise from differential-phase-shift-keyed signals.

In this report, detailed studies are made of the phase and polarization dependence of the inverse MI in a SBF. In the first study (Sec. 3.2), all of the wave frequencies are comparable to the zero-dispersion frequency (ZDF) of the fiber, so the effects of dispersion are unimportant. If the pumps are linearly polarized at  $45^\circ$  to the birefringence axes, a linearly-polarized signal experiences phase-sensitive amplification that does not depend on its polarization angle. However, because dispersion is weak, secondary FWM processes produce a cascade of secondary pumps and secondary signals (idlers) [14, 15, 16]. This cascade consumes bandwidth and depletes the primary pumps. In the second study (Sec. 4.1), most of the wave frequencies are not comparable to the ZDF, so the effects of dispersion are important. Dispersion reduces the FWM cascades, but does not eliminate them completely. Two alternative configurations are considered. In the first configuration, the pump frequencies are far from the ZDF, but the signal frequency is near the ZDF. The presence of a weak cascade does not affect the signal evolution significantly. If the pumps are linearly polarized at  $45^\circ$  to the birefringence axes, the signal still experiences polarization-independent phase-sensitive amplification. In the second configuration, the pump and signal frequencies are all far from the ZDF, but close to each other. Although the signal evolves in a phase-sensitive manner, the presence of a moderate cascade limits the signal amplification significantly.

Studies are also made of nondegenerate FWM processes in which two strong pumps drive weak (signal and idler) sidebands (Sec. 4.2). In phase conjugation (PC), the sum of the sideband frequencies equals the sum of the pump frequencies, whereas in Bragg scattering (BS), the difference between the sideband frequencies equals the difference between the pump frequencies [17]. PC in a SBF provides phase-insensitive amplification, whereas BS in a SBF provides phase-insensitive frequency conversion. Dispersion affects both processes. If the pumps are polarized at  $45^\circ$  to the birefringence axes, signals experience polarization-independent amplification and frequency conversion. The weak cascades that occur do not degrade significantly the properties of PC and BS.

## 2. Wave propagation in a strongly-birefringent fiber

Light-wave propagation in a strongly-birefringent fiber (SBF) is modeled by the coupled Schrödinger equations (CSEs)

$$\partial_z X = i\beta_x(i\partial_\tau)X + i(\gamma_s|X|^2 + \gamma_c|Y|^2)X, \quad (1)$$

$$\partial_z Y = i\beta_y(i\partial_\tau)Y + i(\gamma_c|X|^2 + \gamma_s|Y|^2)Y, \quad (2)$$

where  $z$  is distance,  $\partial_z = \partial/\partial z$ ,  $X$  and  $Y$  are the amplitude (polarization) components of the wave and  $\beta_x$  and  $\beta_y$  are the dispersion functions of the fiber. In the frequency domain

$\beta(\omega) = \sum_{n \geq 1} \beta_n(\omega_c) \omega^n / n!$ , where  $\omega_c$  is the carrier frequency of the wave and  $\omega$  is the difference between the actual and carrier frequencies. To convert from the frequency domain to the time domain one replaces  $\omega$  by  $i\partial_\tau$ , where  $\tau = t - \beta_a z$  is the retarded time and  $\beta_a = [\beta_{1x}(\omega_c) + \beta_{1y}(\omega_c)]/2$  is the average of the group slownesses. The self-nonlinearity coefficient  $\gamma_s = \gamma_K$ , where  $\gamma_K$  is the Kerr coefficient, and the cross-nonlinearity coefficient  $\gamma_c = 2\gamma_K/3$  [18, 19].

### 3. Adjacent waves

Suppose that the wave frequencies are all close to the zero-dispersion frequency (ZDF,  $\omega_0$ ) of the fiber. Then the effects of second- and higher-order dispersion can be neglected. In this (adjacent-wave) case, the CSEs (1) and (2) reduce to the coupled-component equations (CCEs)

$$(\partial_z + \beta_d \partial_t)X = i(\gamma_s |X|^2 + \gamma_c |Y|^2)X, \quad (3)$$

$$(\partial_z - \beta_d \partial_t)Y = i(\gamma_c |X|^2 + \gamma_s |Y|^2)Y, \quad (4)$$

where  $\beta_d = [\beta_{1x}(\omega_c) - \beta_{1y}(\omega_c)]/2$  is the difference between the group slownesses. It follows from Eqs. (3) and (4) that

$$(\partial_z + \beta_d \partial_t)P_x = 0, \quad (5)$$

$$(\partial_z - \beta_d \partial_t)P_y = 0, \quad (6)$$

where the powers  $P_x = |X|^2$  and  $P_y = |Y|^2$ . The power of each component is constant, in a frame moving with the group speed of that component. No power is exchanged between the components. Define the retarded times  $\tau_x = \tau - \beta_d z$  and  $\tau_y = \tau + \beta_d z$ . Then, by using the method of characteristics [20], one finds that

$$X(\tau_x, z) = X(\tau_x, 0) \exp\{i\gamma_s P_x(\tau_x, 0)z + i\gamma_c \int_0^z P_y(\tau_x + 2\beta_d z', 0) dz'\}, \quad (7)$$

$$Y(\tau_y, z) = Y(\tau_y, 0) \exp\{i\gamma_c \int_0^z P_x(\tau_y - 2\beta_d z', 0) dz' + i\gamma_s P_y(\tau_y, 0)z\}. \quad (8)$$

Notice that the formula for  $Y$  can be deduced from the formula for  $X$  by interchanging the subscripts  $x$  and  $y$ , and changing the sign of the walk-off parameter  $\beta_d$ . For multiple-frequency inputs, the self- and cross-nonlinearities in Eqs. (7) and (8) have time-independent parts, which produce self-phase modulation (SPM) and cross-phase modulation (CPM), respectively, and time-dependent parts, which produce scalar and vector FWM. (SPM and scalar FWM involve  $X$  and  $P_x$ , or  $Y$  and  $P_y$ , whereas CPM and vector FWM involve  $X$  and  $P_y$ , or  $Y$  and  $P_x$ .) The effects of SPM and scalar FWM accumulate with distance, as do the effects of CPM. However, the effects of vector FWM, which depend on the integral of a periodic function, are bounded and can be neglected for long distances. Apart from CPM, which only produces time-independent phase shifts, the components evolve nearly independently.

#### 3.1. Phase-insensitive cascade

This general conclusion is reinforced by a specific example. Consider the two-frequency boundary (initial) conditions

$$X(\tau, 0) = \rho_{0x} \exp(i\phi_{0x}) + \rho_{1x} \exp(i\phi_{1x}), \quad (9)$$

$$Y(\tau, 0) = \rho_{0y} \exp(i\phi_{0y}) + \rho_{1y} \exp(i\phi_{1y}), \quad (10)$$

where the phases  $\phi_{jk} = -\omega_j \tau + \phi_{jk}(0)$ . These conditions correspond to two waves (0 and 1) with arbitrary input powers, polarizations and phases. It follows from Eqs. (9) and (10) that

$$P_x(\tau_x, 0) = \rho_{0x}^2 + \rho_{1x}^2 + 2\rho_{0x}\rho_{1x} \cos(\phi_{0x} - \phi_{1x}). \quad (11)$$

$$P_y(\tau_y, 0) = \rho_{0y}^2 + \rho_{1y}^2 + 2\rho_{0y}\rho_{1y} \cos(\phi_{0y} - \phi_{1y}). \quad (12)$$

Each input power has the time average  $\rho_0^2 + \rho_1^2$ , which produces phase shifts, and the contribution  $2\rho_0\rho_1 \cos(\phi_0 - \phi_1)$ , which oscillates at the difference frequency  $\omega_d = \omega_1 - \omega_0$  and produces other frequency components (harmonics). It also follows that

$$\int_0^z P_x(\tau_y - 2\beta_d z, 0) dz' = (\rho_{0x}^2 + \rho_{1x}^2)z - \rho_{0x}\rho_{1x} \{ \sin[\omega_d(\tau_y - 2\beta_d z) - \phi_{dx}] - \sin[\omega_d \tau_y - \phi_{dx}] \} / \beta_d \omega_d. \quad (13)$$

$$\int_0^z P_y(\tau_x + 2\beta_d z, 0) dz' = (\rho_{0y}^2 + \rho_{1y}^2)z + \rho_{0y}\rho_{1y} \{ \sin[\omega_d(\tau_x + 2\beta_d z) - \phi_{dy}] - \sin[\omega_d \tau_x - \phi_{dy}] \} / \beta_d \omega_d, \quad (14)$$

where the phase differences  $\phi_{dj} = \phi_{1j}(0) - \phi_{0j}(0)$ . The time-independent terms in Eqs. (13) and (14) grow linearly with  $z$ , whereas the time-dependent terms are bounded. The relative size of these terms is  $\beta_d \omega_d z$ . The parameters  $\beta_d = 50$  ps/Km (which corresponds to the index difference  $\delta n = 3 \times 10^{-5}$ ),  $\omega_d = 0.3$  Tr/s (which corresponds to the real frequency difference  $f_d = 50$  GHz) and  $z \sim 1$  Km are representative of current experiments. For these parameters,  $\beta_d \omega_d z \sim 15$ , so the time-dependent terms (which produce vector FWM) can be neglected. Similar conclusions apply to multiple-frequency inputs, because the time-dependent contributions to  $P_x$  and  $P_y$  oscillate at the (pairwise) beat frequencies  $\omega_j - \omega_k$ . Notice that the remaining terms do not depend on  $\beta_d$ , so the formulas for  $X$  and  $Y$  are related by the aforementioned interchange of indices. Consequently, only formulas for  $X$  will be stated explicitly in this report.

FWM cascades produced by two inputs were analyzed in [14, 15]. By proceeding as described therein, one can write the output amplitude in the form

$$X(\tau_x, z) = \sum_n X_n(z) \exp(i\phi_{nx} + i\psi_x), \quad (15)$$

where the time-dependent phases

$$\phi_{nx}(\tau_x) = \phi_{0x}(\tau_x) + n[\phi_{1x}(\tau_x) - \phi_{0x}(\tau_x)] \quad (16)$$

and the time-independent phase

$$\psi_x(z) = \gamma_s(\rho_{0x}^2 + \rho_{1x}^2)z + \gamma_c(\rho_{0y}^2 + \rho_{1y}^2)z. \quad (17)$$

The harmonics

$$X_n(z) = i^n \rho_{0x} J_n(\zeta_x) + i^{n-1} \rho_{1x} J_{n-1}(\zeta_x), \quad (18)$$

where the distance variable  $\zeta_x = 2\gamma_s \rho_{0x} \rho_{1x} z$ . The phase of the  $n$ th harmonic depends on the (common) phase reference  $\phi_{0x}$  and the phase difference  $\phi_{1x} - \phi_{0x}$ . However, the power of the harmonic does not depend on either phase. In this sense, each two-input cascade is phase independent. Equations (15)–(18), and their analogs for the  $y$ -components, show that the components of the  $n$ th harmonic have different time-independent phases and their phase modulations arrive at different times.

In general, the powers of the output harmonics depend sensitively on the polarizations of the inputs. However, suppose that the pump amplitudes  $\rho_{0x} = \rho_{0y} = \rho_0$  (so the  $x$ - and  $y$ -polarized processes are driven equally), and the signal amplitudes  $\rho_{1x}, \rho_{1y} \ll \rho_0$ . Then, in the linear regime ( $\zeta_j \ll 1$ ), the signal and primary-idler components

$$X_1 \approx (1 + i\gamma_s \rho_0^2 z) \rho_{1x}, \quad X_{-1} \approx (i\gamma_s \rho_0^2 z) \rho_{1x}. \quad (19)$$

It follows from Eqs. (19), and their analogs for  $Y_1$  and  $Y_{-1}$ , that the signal and primary-idler powers do not depend on the signal polarization (or the pump and signal phases). In this sense, the primary FWM process is signal-polarization independent.

Because solutions (18) and (19) depend on the dimensionless parameters  $\rho/\rho_0$  and  $\gamma_s\rho_0z$ , it is customary to measure the mode powers relative to pump power  $\rho_0^2$  and distance relative to the interaction distance  $1/\gamma_s\rho_0^2$ . However, to facilitate comparisons between theoretical predictions and numerical results, we chose to measure the pump and signal powers relative to a reference power of 1 mW. The cascade produced by a strong pump and a weak signal is illustrated in Fig. 1, for the initial conditions  $\rho_0 = 22.4$ ,  $\rho_{1x} = 0.283$  and  $\rho_{1y} = 0.141$ . The input spectrum ( $\gamma_s\rho_0^2z = 0$ ) is shown in Fig. 1(a). The pump is polarized at  $45^\circ$  to the slow ( $x$ ) axis of the fiber, whereas the signal is polarized at about  $27^\circ$ . The output spectrum ( $\gamma_s\rho_0^2z = 10$ ) is shown in Fig. 1(b). Not only has the signal been amplified by 20 dB, but a primary idler has also been generated, whose power is comparable to the signal power. The 6-dB difference between the  $x$  and  $y$  components of the output signal and primary idler equals the difference between the components of the input signal. This result shows that both polarizations are amplified by the same amount: In the linear regime signal amplification and idler generation are polarization independent. However, the differences between the components of the neighboring idlers are 12 dB, which shows that the generation of secondary idlers is polarization dependent.

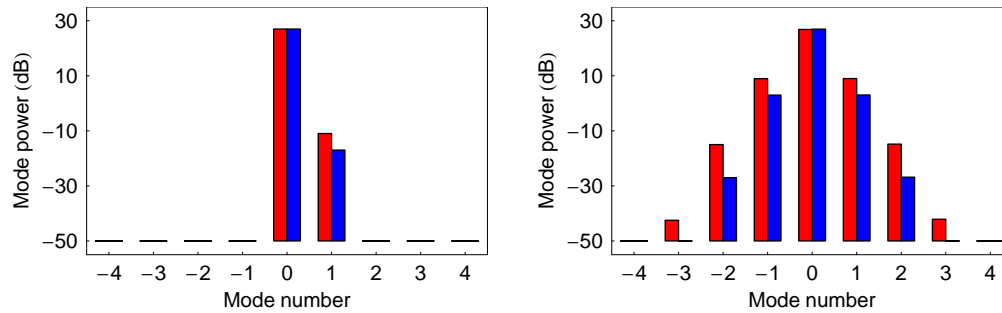


Fig. 1. Normalized mode powers [Eq. (18)] plotted as functions of mode number for the case in which  $\rho_0 = 22.4$ ,  $\rho_{1x} = 0.283$  and  $\rho_{1y} = 0.141$ : (a)  $\gamma_s\rho_0^2z = 0.0$  and (b)  $\gamma_s\rho_0^2z = 10.0$ . Red bars denote  $x$  components, whereas blue bars denote  $y$  components.

To test the theoretical predictions, we made numerical simulations based on the CSEs (1) and (2), for  $\beta_3 = 0.03 \text{ ps}^3/\text{Km}$ ,  $\beta_4 = -3 \times 10^{-4} \text{ ps}^4/\text{Km}$  and  $\gamma_s = 10/\text{Km}\cdot\text{W}$ . The pump powers  $P_x = P_y = 0.5 \text{ W}$  and the signal powers  $P_{sx} = 0.08$  and  $P_{sy} = 0.02 \text{ mW}$  (which correspond to the pump and signal amplitudes of Fig. 1). The pump frequency was the ZDF and the signal-

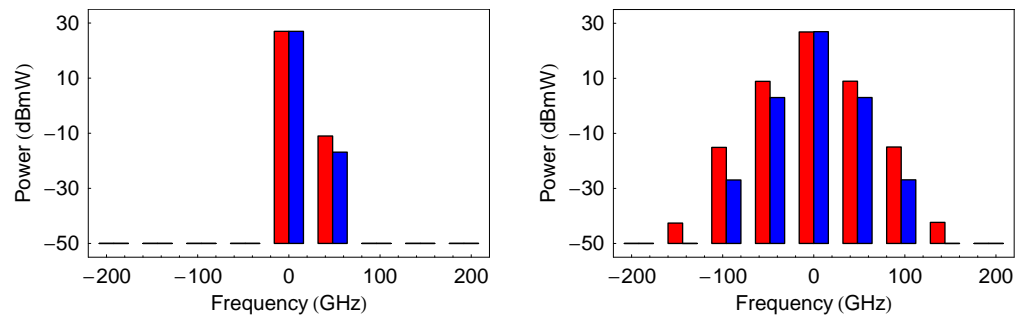


Fig. 2. (a) Simulated mode powers [Eqs. (1) and (2)] plotted as functions of frequency for the case in which the pump powers  $P_x = P_y = 0.5 \text{ W}$  and the signal powers  $P_{sx} = 0.08$  and  $P_{sy} = 0.02 \text{ mW}$ : (a)  $z = 0 \text{ Km}$  and (b)  $z = 2.0 \text{ Km}$ . Red bars denote  $x$  components, whereas blue bars denote  $y$  components.

pump frequency difference was 0.31 Tr/s (50 GHz), which is typical of 10-Gb/s communication systems. The simulation results, which are shown in Fig. 2, confirm the theoretical predictions.

In Fig. 3, the simulated signal and idlers gains are plotted as functions of the (input) signal polarization  $[\tan^{-1}(\rho_{1y}/\rho_{1x})]$ , for the same parameters as Fig. 2. The gain variations are about  $\pm 1\%$ , so the gain is nearly polarization independent, as predicted.

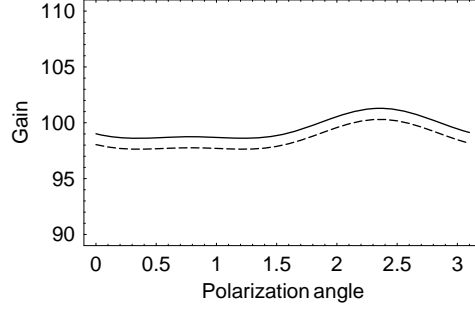


Fig. 3. Simulated gain [Eqs. (1) and (2)] of the signal (solid curve) and idler (dashed curve) plotted as functions of the signal polarization, for the same parameters as Fig. 2.

### 3.2. Phase-sensitive cascade

Now consider the three-frequency input conditions

$$X(\tau, 0) = \rho \exp(i\phi_{-1}) + \rho_{0x} \exp(i\phi_0) + \rho \exp(i\phi_1). \quad (20)$$

These conditions correspond to two strong pumps ( $-1$  and  $1$ ), which are linearly polarized (LP) at  $45^\circ$  to the birefringence axes, and a weak signal ( $0$ ), which is LP at an arbitrary angle. The pump powers are equal and the signal frequency is the average of the pump frequencies  $[\omega_0 = (\omega_1 + \omega_{-1})/2]$ . This process is called the inverse modulation interaction (MI). Define the frequency difference  $\omega_d = (\omega_1 - \omega_{-1})/2$ , the phase average  $\phi_a = [\phi_1(0) + \phi_{-1}(0)]/2$  and the phase difference  $\phi_d = [\phi_1(0) - \phi_{-1}(0)]/2$ . Then, by measuring frequency relative to the average frequency  $\omega_0$ , phase relative to the reference phase  $\phi_a$ , and time relative to the reference time  $\phi_d/\omega_d$ , one can rewrite condition (20) in the simpler form

$$X(\tau, 0) = \rho \exp(i\omega_d \tau_x) + \rho_{0x} \exp(i\phi_0) + \rho \exp(-i\omega_d \tau_x), \quad (21)$$

where  $\phi_0$  is the input phase.

FWM cascades produced by three inputs were also analyzed in [14, 15]. By proceeding as described therein, one can write the output amplitude in the form

$$X(\tau_x, z) = \sum_n X_n(z) \exp[-in\omega_d \tau_x + i\psi_x], \quad (22)$$

where the time-independent phase

$$\psi_x = 2(\gamma_s + \gamma_c)\rho^2 z + (\gamma_s \rho_{0x}^2 + \gamma_c \rho_{0y}^2)z, \quad (23)$$

and the harmonics

$$X_n(\zeta) = \sum_m i^{n-m} J_m(\zeta) [\rho_{0x} \exp(i\phi_0) J_{n-2m}(\epsilon_x \zeta) - 2i\rho J'_{n-2m}(\epsilon_x \zeta)], \quad (24)$$

where  $\zeta = 2\rho^2 z$ ,  $\varepsilon_x = 2(\rho_{0x}/\rho) \cos \phi_0$  and  $J'_l(y) = dJ_l(y)/dy$ . Equation (24) and its analog for  $Y_n$  show that the output harmonics depend on the polarization of the input signal in two ways: First, because  $\gamma_s \neq \gamma_c$ , their components experience different phase shifts. Second, their components depend nonlinearly on  $\varepsilon_j$  ( $\rho_{0j}$ ). However, in the linear regime ( $\varepsilon_j \zeta \ll 1$ ), the signal-induced phase shifts are negligible, the pumps (odd harmonics) do not depend on  $\rho_{0j}$ , and the signal and idlers (even harmonics) are all proportional to  $\rho_{0j}$ . In this regime, the exact solution (24) reduces to the approximate solution

$$X_n(\zeta) \approx i^{n/2} \rho_{0x} \{J_{n/2}(\zeta) [\exp(i\phi_0) + 2i\zeta \cos \phi_0] + J'_{n/2}(\zeta) 2\zeta \cos \phi_0\}, \quad (25)$$

where  $n$  is even. Every contribution to  $X_n$  is proportional to  $\rho_{0x}$ , so every contribution to  $Y_n$  is proportional to  $\rho_{0y}$ . Both components have the same dependence on  $\phi_0$ . Hence, the output signal and idler powers depend on the input signal phase, but not the input signal polarization: In the linear regime, polarization-independent phase-sensitive amplification is possible.

For the signal mode (0), Eq. (25) can be written in the input-output form

$$X_0(\zeta) = \rho_0 [\mu(\zeta) \exp(i\phi_0) + \nu(\zeta) \exp(-i\phi_0)], \quad (26)$$

where the transfer functions  $\mu(\zeta) = J_0(\zeta) + \zeta J'_0(\zeta) + i\zeta J_0(\zeta)$  and  $\nu(\zeta) = \zeta J'_0(\zeta) + i\zeta J_0(\zeta)$ . The signal power attains its extremal values when  $2\phi_m = \tan^{-1}[(\mu_r \nu_i - \mu_i \nu_r)/(\mu_r \nu_r + \mu_i \nu_i)]$ , where the subscripts  $r$  and  $i$  denote real and imaginary parts, respectively. The first-quadrant value of  $2\phi_m$  corresponds to the maximal gain  $(|\mu| + |\nu|)^2$ , whereas the third-quadrant value corresponds to the minimal gain  $(|\mu| - |\nu|)^2$ . By using the aforementioned formulas for the transfer functions, one finds that

$$2\phi_m(\zeta) = \tan^{-1} \left\{ \frac{J_0^2(\zeta)}{\zeta [J_0^2(\zeta) + J_1^2(\zeta)] - J_0(\zeta) J_1(\zeta)} \right\}. \quad (27)$$

The signal gain is plotted as a function of (input) signal phase and distance in Fig. 4. For short distances the gain is maximal when the input phase  $\phi_0 \approx \pi/4$ , whereas it is minimal when  $\phi_0 \approx 3\pi/4$ . As the distance increases, the phases required for maximal and minimal gain tend nonmonotonically to 0 and  $\pi/2$ , respectively [Fig. 4(a)]. For  $\gamma_s \rho^2 z = 2$  the aforementioned phases are 0.124 and 1.69, respectively [Fig. 4(b)].

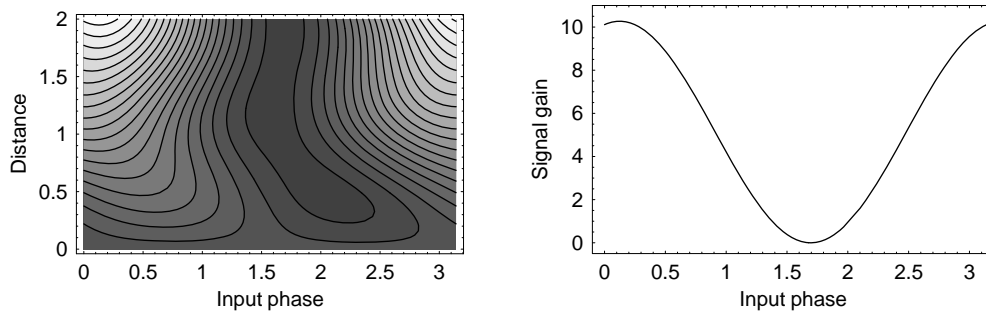


Fig. 4. (a) Signal gain [Eq. (26)] plotted as a function of signal phase and distance ( $\gamma_s \rho^2 z$ ). Light and dark regions correspond to high and low gains, respectively. The contour spacing is 0.5. (b) Gain plotted as a function of phase for the case in which  $\gamma_s \rho^2 z = 2.0$ .

The cascades produced by two strong pumps and a weak signal are illustrated in Figs. 5 and 6, for cases in which  $\rho = 22.4$  and  $\rho_0 = 0.316$ . The input spectrum is shown in Fig. 5(a). The

output spectra for  $\phi_0 = 0.124$  and  $1.69$  are shown in Figs. 6(a) and 6(b) respectively. In the former case the signal was amplified by 10 dB, whereas in the latter it was attenuated by 35 dB. Despite the presence of many secondary pumps (even modes) and idlers (odd modes), the signal experiences significant phase-sensitive amplification and attenuation [14].

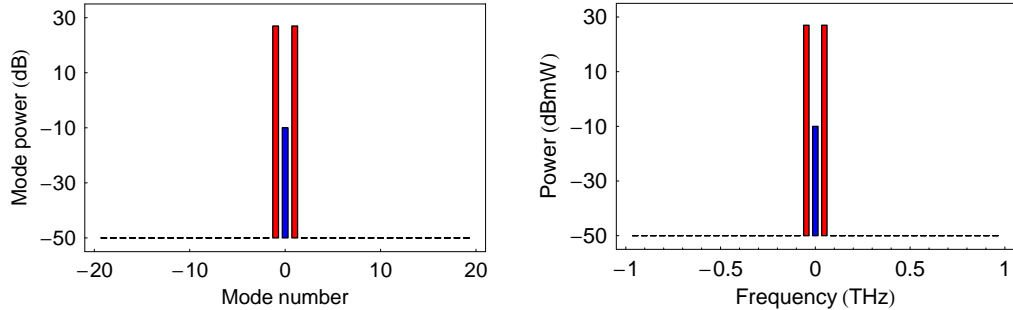


Fig. 5. Input power plotted as a function of mode number (frequency) for the case in which there are two pumps and one signal. (a)  $\rho = 22.4$  and  $\rho_0 = 0.316$ . (b)  $P = 0.5$  W and  $P_0 = 0.1$  mW. Red bars represent the odd harmonics (pumps), whereas blue bars represent the even harmonic (signal).

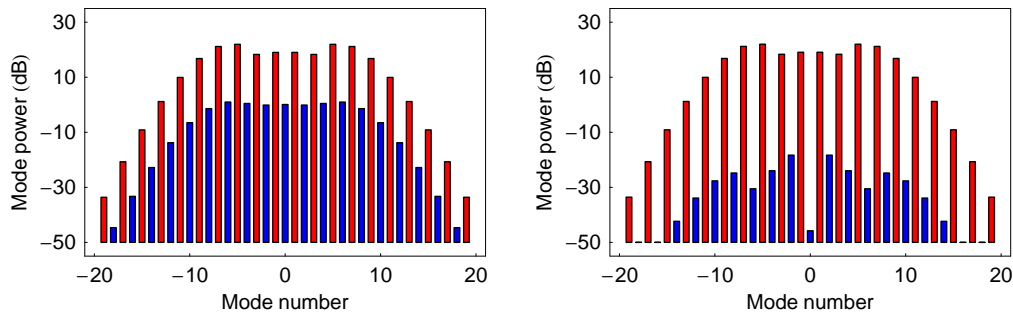


Fig. 6. Normalized mode power [Eq. (24)] plotted as a function of mode number for cases in which  $\rho = 22.4$ ,  $\rho_0 = 0.316$  and  $\gamma_s \rho^2 z = 2.0$ . (a) For  $\phi_0 = 0.124$  the signal is amplified by 10 dB. (b) For  $\phi_0 = 1.69$  the signal is attenuated by 35 dB. Red bars represent the odd harmonics (pumps), whereas blue bars represent the even harmonics (signal and idlers).

To test the theoretical predictions, we made scalar (one-polarization) and vector (two-polarization) simulations based on Eqs. (1) and (2), for  $\beta_3 = 0.03$  ps<sup>3</sup>/Km,  $\beta_4 = -3 \times 10^{-4}$  ps<sup>4</sup>/Km and  $\gamma_s = 10$ /Km-W. The pump powers  $P_x = P_y = 0.5$  W and the signal powers  $P_{sx} = 0.08$  and  $P_{sy} = 0.02$  mW (which correspond to the pump and signal amplitudes of Fig. 6). The average pump frequency was the ZDF, and the signal-pump frequency difference was 0.31 Tr/s (50 GHz). The simulation results are shown in Fig. 7. For amplification, the theoretical predictions and numerical results agree quantitatively [Figs. 6(a) and 7(a)], whereas for attenuation, they agree qualitatively [Figs. 6(b) and 7(b)]. Each harmonic in a cascade is continuously augmented or diminished by FWM processes. For the signal to be attenuated significantly, the processes that affect it must all diminish it simultaneously (cancel perfectly). Small amounts of dispersion (which are present in the simulations), modify these processes slightly and prevent this perfect cancellation. Overall, the simulation results confirm the theoretical predictions. Significant phase-sensitive amplification and attenuation was observed in a recent experiment [16], in which the inverse MI was used to phase-regenerate a signal.

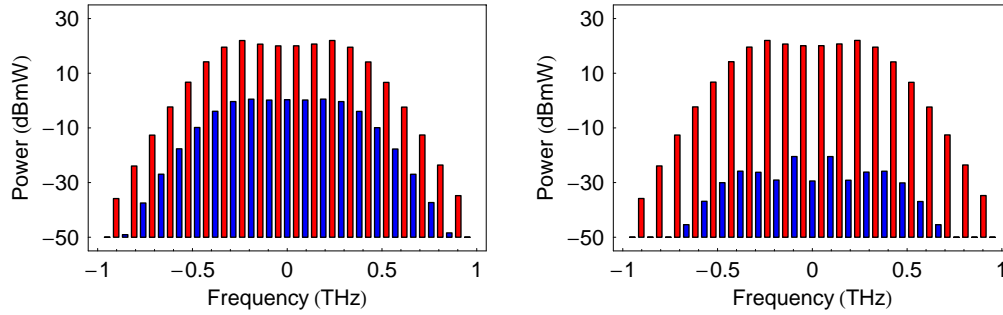


Fig. 7. Simulated mode power [Eq. (1)] plotted as a function of mode frequency for cases in which  $P = 0.5$  W,  $P_0 = 0.1$  mW and  $z = 0.4$  Km. (a) For  $\phi_0 = 0.124$  the signal is amplified by 10 dB. (b) For  $\phi_0 = 1.69$  the signal is attenuated by 20 dB.

In Fig. 8 the simulated signal gain is plotted as a function of (input) signal phase and polarization [ $\tan^{-1}(\rho_{0y}/\rho_{0x})$ ], for the same parameters as Fig. 7. The phase dependence is nearly independent of polarization [Fig. 8(a)], and the polarization dependence is weak for the phases associated with maximal amplification and attenuation [Fig. 8(b)]. Thus, the gain is nearly polarization independent, as predicted.

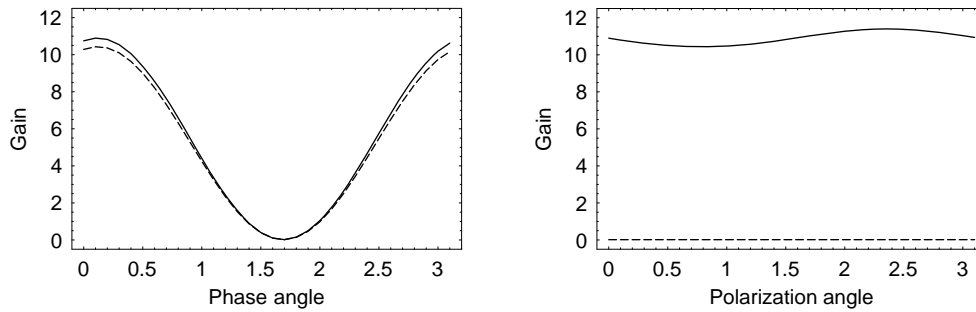


Fig. 8. (a) Simulated signal gain [Eq. (1)] plotted as a function of signal phase for the signal polarizations  $\theta = 0$  (solid curve) and  $\theta = \pi/4$  (dashed curve). (b) Simulated gain [Eqs. (1) and (2)] plotted as a function of polarization for the phases  $\phi = 0.124$  (solid curve) and  $\phi = 1.69$  (dashed curve). The other parameters are the same as those of Fig. 7.

The ZDFs of real fibers vary with distance [21]. Phase-sensitive cascades should be affected only weakly by ZDF variations, because the frequencies of the harmonics are all close to the average ZDF. Although dispersion varies with distance, it remains weak at these frequencies.

#### 4. Distant waves

Now suppose that the wave frequencies are not all close to the ZDF or each other. Then the effects of dispersion must be included. In this (distant-wave) case, one uses separate equations for each polarization and frequency component to study the wave interaction. Consider the interaction of four waves (1–4). By substituting the ansätze

$$X(t, z) = \sum_{j=1}^4 X_j(z) \exp(-i\omega_j t), \quad (28)$$

$$Y(t, z) = \sum_{j=1}^4 Y_j(z) \exp(-i\omega_j t) \quad (29)$$

in the CSEs (1) and (2), and collecting terms of like frequency, one finds that

$$\begin{aligned}
\partial_z X_1 &= i\beta_x(\omega_1)X_1 + i\gamma_s(|X_1|^2 + 2|X_2|^2 + 2|X_3|^2 + 2|X_4|^2)X_1 \\
&\quad + i\gamma_s X_3^* X_2^2 + i2\gamma_s X_4^* X_2 X_3 \\
&\quad + i\gamma_c(|Y_1|^2 + |Y_2|^2 + |Y_3|^2 + |Y_4|^2)X_1 + i\gamma_c Y_1(Y_2^* X_2 + Y_3^* X_3 + Y_4^* X_4) \\
&\quad + i\gamma_c Y_3^* Y_2 X_2 + i\gamma_c Y_4^*(Y_2 X_3 + Y_3 X_2), \tag{30}
\end{aligned}$$

$$\begin{aligned}
\partial_z X_2 &= i\beta_x(\omega_2)X_2 + i\gamma_s(|X_2|^2 + 2|X_3|^2 + 2|X_4|^2 + 2|X_1|^2)X_2 \\
&\quad + i2\gamma_s X_2^* X_3 X_1 + i\gamma_s X_4^* X_3^2 + i2\gamma_s X_3^* X_4 X_1 \\
&\quad + i\gamma_c(|Y_2|^2 + |Y_3|^2 + |Y_4|^2 + |Y_1|^2)X_2 + i\gamma_c Y_2(Y_3^* X_3 + Y_4^* X_4 + Y_1^* X_1) \\
&\quad + i\gamma_c Y_2^*(Y_3 X_1 + Y_1 X_3) + i\gamma_c Y_4^* Y_3 X_3 + i\gamma_c Y_3^*(Y_4 X_1 + Y_1 X_4). \tag{31}
\end{aligned}$$

Equations (30) and (31) apply to the special case in which  $\omega_2 - \omega_1 = \omega_3 - \omega_2 = \omega_4 - \omega_3$ . Similar equations apply to the general case in which the frequencies are arbitrary. One can deduce the equations for  $Y_1$  and  $Y_2$  from Eqs. (30) and (31), respectively, by interchanging  $X_j$  and  $Y_j$ . One can also deduce the equations for  $A_3$  and  $A_4$  from the equations for  $A_1$  and  $A_2$  by interchanging 1 and 4, and 2 and 3, respectively. ( $A$  is  $X$  or  $Y$ .) Collectively, these equations are called the coupled-mode equations (CMEs).

The first term on the right side of Eq. (30) represents a linear phase shift, caused by dispersion, whereas the second and fifth terms represent nonlinear phase shifts, caused by SPM and CPM. The third and fourth terms represent scalar FWM processes in which  $2\pi_{2x} \leftrightarrow \pi_{3x} + \pi_{1x}$  and  $\pi_{2x} + \pi_{3x} \leftrightarrow \pi_{4x} + \pi_{1x}$ , respectively, where  $\pi_{jk}$  represents a photon with frequency  $\omega_j$  that is polarized parallel to the  $k$ -axis. The seventh term represents the vector FWM process in which  $\pi_{2x} + \pi_{2y} \leftrightarrow \pi_{3y} + \pi_{1x}$ , and the eighth term represents the vector FWM processes in which  $\pi_{2y} + \pi_{3x} \leftrightarrow \pi_{4y} + \pi_{1x}$  and  $\pi_{2x} + \pi_{3y} \leftrightarrow \pi_{4y} + \pi_{1x}$ . The sixth term represents a processes in which  $\pi_{1x} + \pi_{2y} \leftrightarrow \pi_{1y} + \pi_{2x}$ , and similar processes that involve waves 3 and 4. Analyses show that these processes are cross-polarization rotations (CPRs). Similar statements apply to the terms in Eq. (31).

Define the total  $x$ - and  $y$ -polarized powers  $P_x = \sum_{j=1}^4 |X_j|^2$  and  $P_y = \sum_{j=1}^4 |Y_j|^2$ , respectively. Phase shifts do not change  $P_x$  and  $P_y$ . Scalar-FWM processes exchange energy between different  $x$ -polarized components or different  $y$ -polarized components. The photon-exchange equations show that, in each CPR and vector-FWM process,  $x$ - and  $y$ -polarized photons are destroyed and other  $x$ - and  $y$ -polarized photons are created. Hence, the CMEs conserve  $P_x$  and  $P_y$ , as do the coupled-component equations (CCEs) of Sec. 3. Power conservation is discussed in detail in the Appendix.

For parameters that are typical of many experiments,  $\beta(\omega) = \sum_{n \geq 1} \beta_n \omega^n / n! \approx \beta_1 \omega$ , where  $\omega$  is the frequency of any wave (measured relative to a reference frequency, such as the ZDF). Let  $X_j(z) = \bar{X}_j(z) \exp(i\beta_{1x} \omega_j z)$  and  $Y_j(z) = \bar{Y}_j(z) \exp(i\beta_{1y} \omega_j z)$ , where  $\beta_{1x} = \beta_d$  and  $\beta_{1y} = -\beta_d$ . By making these substitutions in Eqs. (30) and (31), one obtains modified equations for  $\bar{X}_j$  and  $\bar{Y}_j$ . The SPM and CPM terms in Eq. (30) are unaffected by this change of variables. The scalar FWM terms are multiplied by the phase factors  $\exp[i\beta_d(2\omega_2 - \omega_3 - \omega_1)]$  and  $\exp[i\beta_d(\omega_2 + \omega_3 - \omega_4 - \omega_1)]$ , both of which equal unity (because the frequency-matching conditions are satisfied by assumption). The CPR terms are multiplied by the phase factors  $\exp[i2\beta_d(\omega_j - \omega_1)]$ , the spatial average of which is zero. The vector FWM terms are multiplied by the phase factors  $\exp[-i\beta_d(\omega_3 - \omega_1)]$ ,  $\exp[-i2\beta_d(\omega_3 - \omega_1)]$  and  $\exp[-i2\beta_d(\omega_2 - \omega_1)]$ , the averages of which are zero. Similar statements apply to the terms in the modified version of Eq. (31). Hence, one can replace Eqs. (30) and (31) by the reduced equations

$$\begin{aligned}
\partial_z X_1 &\approx i\beta_x(\omega_1)X_1 + i\gamma_s(|X_1|^2 + 2|X_2|^2 + 2|X_3|^2 + 2|X_4|^2)X_1 \\
&\quad + i\gamma_s X_3^* X_2^2 + i2\gamma_s X_4^* X_2 X_3
\end{aligned}$$

$$+ i\gamma_c(|Y_1|^2 + |Y_2|^2 + |Y_3|^2 + |Y_4|^2)X_1, \quad (32)$$

$$\begin{aligned} \partial_z X_2 \approx & i\beta_x(\omega_2)X_2 + i\gamma_s(|X_2|^2 + 2|X_3|^2 + 2|X_4|^2 + 2|X_1|^2)X_2 \\ & + i2\gamma_s X_2^* X_3 X_1 + i\gamma_s X_4^* X_3^2 + i2\gamma_s X_3^* X_4 X_1 \\ & + i\gamma_c(|Y_2|^2 + |Y_3|^2 + |Y_4|^2 + |Y_1|^2)X_2. \end{aligned} \quad (33)$$

where the dispersion functions  $\beta(\omega) = \sum_{n \geq 2} \beta_n \omega^n / n!$  contain only second- and higher-order dispersion terms, and the bars were omitted for simplicity.

As stated above, the total powers  $P_x$  and  $P_y$  are conserved. Let  $X_j(z) = \hat{X}_j(z) \exp[i(2\gamma_s P_x + \gamma_c P_y)z]$  and  $Y_j(z) = \hat{Y}_j(z) \exp[i(\gamma_c P_x + 2\gamma_s P_y)z]$ . For each polarization, every frequency component has the same phase shift. By making these substitutions in Eqs. (32) and (33), one removes the terms that produce this common shift, and obtains the reduced equations

$$\partial_z X_1 \approx i\beta_x(\omega_1)X_1 - i\gamma_s |X_1|^2 X_1 + i\gamma_s X_3^* X_2^2 + i2\gamma_s X_4^* X_2 X_3, \quad (34)$$

$$\partial_z X_2 \approx i\beta_x(\omega_2)X_2 - i\gamma_s |X_2|^2 X_2 + i2\gamma_s X_2^* X_3 X_1 + i\gamma_s X_4^* X_3^2 + i2\gamma_s X_3^* X_4 X_1, \quad (35)$$

where the carets were omitted for simplicity. Equations (34) and (35) describe scalar FWM processes in which  $2\pi_{2x} \leftrightarrow \pi_{3x} + \pi_{1x}$ ,  $\pi_{2x} + \pi_{3x} \leftrightarrow \pi_{4x} + \pi_{1x}$  and  $2\pi_{3x} \leftrightarrow \pi_{4x} + \pi_{2x}$ . Similar equations apply to the y-components of waves 1 and 2, and the x- and y-components of waves 3 and 4. These reduced CMEs imply that the x- and y-components of the waves evolve independently. Similar (reduced) CMEs can be derived for larger collections of waves (harmonics).

Equations (34) and (35) do not describe the vector FWM process associated with the seventh term on the right side of Eq. (30) and the eighth term on the right side of Eq. (31). In this process, which is often called the CPM instability [22, 23], a pump polarized at  $45^\circ$  to the birefringence axes drives an x-polarized sideband and a y-polarized sideband. Let  $\omega$  denote the frequency difference between the x-polarized sideband and the pump. Then the dispersive contribution to the wavenumber mismatch is  $(\beta_{1x} - \beta_{1y})\omega + (\beta_{2x} + \beta_{2y})\omega^2/2$ . Phase matching only occurs for large frequency differences, for which the first two terms in the dispersion functions have the same magnitude. We omitted such frequencies from our analysis.

It is instructive to analyze the initial evolution of the FWM processes described by Eqs. (34) and (35). First, consider the MI  $2\pi_2 \rightarrow \pi_3 + \pi_1$ , in which two photons from a strong pump (2) are destroyed and two sideband, or signal and idler, photons (3 and 1) are created ( $\pi_j$  is an abbreviation for  $\pi_{jx}$ ). By linearizing Eqs. (34) and (35), one obtains the input–output equations

$$X_1(z) = \mu(z)X_1(0) + \nu(z)X_3^*(0), \quad (36)$$

$$X_3^*(z) = \nu^*(z)X_1(0) + \mu^*(z)X_3^*(0). \quad (37)$$

In Eqs. (36) and (37), the transfer functions

$$\mu(z) = \cos(kz) + i(\delta/k) \sin(kz), \quad (38)$$

$$\nu(z) = i(\tilde{\gamma}/k) \sin(kz), \quad (39)$$

where the wavenumber-mismatch parameter  $\delta = [\beta(\omega_3) + \beta(\omega_1) - 2\beta(\omega_2)]/2 + \gamma_s P_2$ , the coupling parameter  $\tilde{\gamma} = \gamma_s P_2$  and the MI wavenumber  $k = (\delta^2 - \tilde{\gamma}^2)^{1/2}$ . The MI is unstable (amplifies the signal) whenever  $\tilde{\gamma} > |\delta|$ . If the modulation frequency  $\omega_2 - \omega_1$  is low, only second-order dispersion is important and the instability criterion requires the pump frequency to be in the anomalous-dispersion regime [ $\beta_2(\omega_2) < 0$ ]. The effects of higher-order dispersion on the existence and frequency dependence of MI gain are discussed in [17].

Second, consider the inverse MI  $\pi_3 + \pi_1 \rightarrow 2\pi_2$ , in which photons from two strong pumps (3 and 1) are destroyed and two signal photons (2) are created. The inverse MI is characterized by the input–output equation

$$X_2(z) = \mu(z)X_2(0) + \nu(z)X_2^*(0), \quad (40)$$

where the transfer functions were defined in Eqs. (38) and (39),  $\delta = [2\beta_2(\omega_2) - \beta(\omega_3) - \beta(\omega_1)]/2 + \gamma_s(P_1 + P_3)/2$  and  $\bar{\gamma} = 2\gamma_s(P_1P_3)^{1/2}$ . The inverse MI is also unstable whenever  $\bar{\gamma} > |\delta|$ . When one compares the formulas for the MI and inverse MI, one finds that the dispersive contributions to the mismatch parameters have opposite signs and the coupling parameters differ by a factor of 2. Hence, if the modulation frequency is low, the inverse MI exists when the pump frequency is in the anomalous- and normal-dispersion regimes, but is most unstable when the pump frequency is in the latter [ $\beta_2(\omega_2) > 0$ ].

Third, consider the PC process  $\pi_2 + \pi_3 \rightarrow \pi_4 + \pi_1$ , in which photons from two strong pumps (2 and 3) are destroyed, and signal and idler photons (4 and 1) are created. PC is characterized by the input–output equations

$$X_1(z) = \mu(z)X_1(0) + v(z)X_4^*(0), \quad (41)$$

$$X_4^*(z) = v^*(z)X_1(0) + \mu^*(z)X_4^*(0), \quad (42)$$

where the transfer functions were defined in Eqs. (38) and (39),  $\delta = [\beta(\omega_4) + \beta(\omega_1) - \beta_2(\omega_2) - \beta(\omega_3)]/2 + \gamma_s(P_2 + P_3)/2$  and  $\bar{\gamma} = 2\gamma_s(P_2P_3)^{1/2}$ . PC is also unstable whenever  $\bar{\gamma} > |\delta|$ . It is most unstable when the average of the pump frequencies is in the anomalous-dispersion regime [ $\beta_2(\omega_a) > 0$ , where  $\omega_a = (\omega_2 + \omega_3)/2$ ]. Frequency tuning in the presence of higher-order dispersion is discussed in [17, 24].

Fourth, consider the BS process  $\pi_2 + \pi_3 \rightarrow \pi_4 + \pi_1$ , in which photons from a strong pump (3) and a weak signal (2) are destroyed, and pump (1) and idler (4) photons are created. Although the photon-exchange equations for BS and PC have the same form, the identities of the pumps and sidebands are different. BS is characterized by the input–output equations

$$X_2(z) = \mu(z)X_2(0) + v(z)X_4(0), \quad (43)$$

$$X_4(z) = -v^*(z)X_2(0) + \mu^*(z)X_4(0), \quad (44)$$

where the transfer functions were defined in Eqs. (38) and (39),  $\delta = [\beta(\omega_2) + \beta(\omega_3) - \beta_4(\omega_2) - \beta(\omega_1)]/2 + \gamma_s(P_1 - P_3)/2$ ,  $\bar{\gamma} = 2\gamma_s(P_1P_3)^{1/2}$  and  $k = (\delta^2 + \bar{\gamma}^2)^{1/2}$ . BS is always stable: It provides coupling, but no amplification. If the pump powers are equal ( $P_1 = P_3$ ), a complete transfer of power from the signal to the idler occurs when the average of the signal frequency and the higher pump frequency equals the ZDF [ $\omega_a = \omega_0$ , where  $\omega_a = (\omega_2 + \omega_3)/2$ ]. If the pump powers are not equal, a complete power transfer is possible when the average frequency is in either dispersion regime. Frequency tuning in the presence of higher-order dispersion is discussed in [25].

#### 4.1. Phase-sensitive amplification

It was shown in Sec. 3.2 that the inverse MI of pumps whose frequencies are near the ZDF provides polarization-independent phase-sensitive amplification. However, because dispersion is weak near the ZDF, secondary FWM processes produce secondary pumps and idlers, which consume bandwidth and deplete the primary pumps. One can suppress the generation of secondary products by using primary pumps whose frequencies are far from the ZDF [17] (and it was for such a frequency configuration that inverse MI was proposed [12]). Equations (38)–(40) were used to model the inverse MI for the fiber parameters  $\beta_3 = 0.03 \text{ ps}^3/\text{Km}$ ,  $\beta_4 = -3 \times 10^{-4} \text{ ps}^4/\text{Km}$ ,  $\gamma = 10/\text{Km-W}$  and  $l = 0.46 \text{ Km}$ , and the pump powers  $P_1 = P_3 = 0.25 \text{ W}$ . (The slowness parameter  $\beta_1$  has no effect on the inverse MI when the waves are co-polarized.) The dependence of the inverse MI on the pump and signal frequencies was studied. In Fig. 9, the signal gain is plotted as a function of the signal phase, for the pump frequencies  $\omega_1 = -8.25$  and  $\omega_3 = 11.75 \text{ Tr/s}$ , and the signal frequency  $\omega_2 = 1.75 \text{ Tr/s}$ . These frequencies are measured relative to the ZDF. (Relative to the signal, the pump frequencies are  $\pm\omega_a$ , where the frequency

difference  $\omega_d = 10$  Tr/s.) For reference, the dispersion coefficient  $\beta_2(\omega_2) = 0.052$ . The inverse-MI equation (40) predicts that the signal gain  $P_2(z)/P_2(0)$  will attain a maximum of 20 dB when the signal phase  $\phi_2(0) = 0.78$ , and a minimum of  $-20$  dB when  $\phi_2 = 2.32$ .

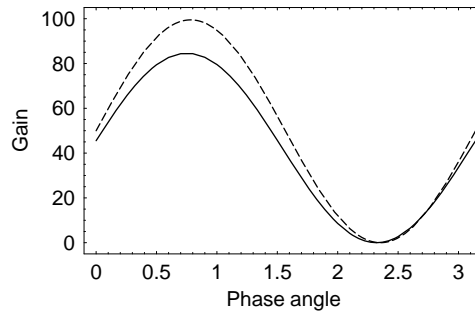


Fig. 9. Signal gain plotted as a function of signal phase, for the fiber length  $l = 0.46$  Km, the pump powers  $P_1 = P_3 = 0.25$  W and the signal power  $P_2 = 0.1$  mW. The pump frequencies are  $-1.31$  and  $1.87$  THz, and the signal frequency is  $0.28$  THz. The dashed curve denotes the theoretical prediction [Eq. (40)], whereas the solid curve denotes the simulation result [Eq. (1)].

To test these predictions, we made scalar simulations based on Eq. (1), for the aforementioned parameters and the signal power  $P_2(0) = 0.1$  mW. In these simulations, a gain maximum of 19.3 dB was attained for  $\phi_2 = 0.78$  and a minimum of  $-19.3$  dB was attained for  $\phi_2 = 2.35$ , as shown in Fig. 9. The theoretical predictions agree quite well with the simulation results.

The small discrepancies between the theoretical and numerical results are due to the presence of weak FWM cascades. In Fig. 10, the simulated mode power [Eq. (1)] is plotted as a function of frequency (measured relative to the signal frequency), for the parameters of Fig. 9. In Fig. 10(a), for which  $\phi_2 = 0.78$ , the amplified signal (9.3 dBmW) is stronger than its idlers (about  $-5$  dBmW), whereas in Fig. 10(b), for which  $\phi_2 = 2.32$ , the attenuated signal ( $-29.3$  dBmW) is weaker than its idlers (about  $-25$  dBmW). Pump-pump FWM does not involve the signal (and is intrinsically phase-insensitive), so the secondary pump powers are the same in both figures (about  $-10$  dB).

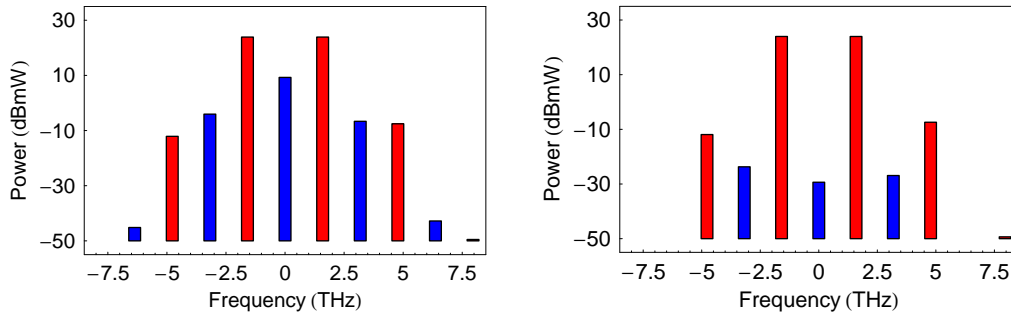


Fig. 10. Simulated mode power [Eq. (1)] plotted as a function of mode frequency (measured relative to the signal frequency), for the parameters of Fig. 9. (a) When the signal phase  $\phi_2 = 0.78$ , the signal is amplified by 19.3 dB. (b) When  $\phi_2 = 2.35$ , the signal is attenuated by 19.3 dB. Red bars denote odd harmonics (pumps), whereas blue bars denote even harmonics (signal and idlers).

To study the polarization dependence of the inverse MI, we made vector simulations based on Eqs. (1) and (2), for the parameters of Fig. 9. The signal gain is plotted as a function of the signal polarization in Fig. 11. For  $\phi_2 = 0.78$  the amplification varies by  $\pm 0.04$  dB, whereas for  $\phi_2 = 2.35$  the attenuation varies by  $\pm 0.03$  dB. Hence, polarization-independent (phase-sensitive) amplification is possible in a SBF, if the pump frequencies are dissimilar.

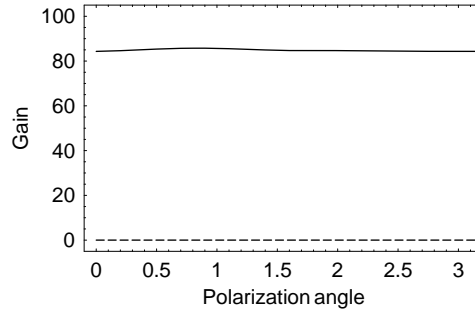


Fig. 11. Simulated signal gain [Eqs. (1) and (2)] plotted as a function of signal polarization, for the parameters of Fig. 9. The solid curve represents the signal phase  $\phi_2 = 0.78$ , whereas the dashed curve represents  $\phi_2 = 2.35$ .

One can also suppress the generation of secondary pumps by using primary pumps and a signal, whose frequencies are all far from the ZDF (but not necessarily each other). The predictions of the three-mode model of inverse MI [Eq. (40)] are shown in Fig. 12(a), for the parameters  $\beta_2 = 5.0$  ps<sup>2</sup>/Km,  $\beta_3 = 0.03$  ps<sup>3</sup>/Km,  $\beta_4 = -3 \times 10^{-4}$  ps<sup>4</sup>/Km,  $\gamma_s = 10$  /Km-W,  $l = 0.46$  Km,  $P_x = 0.25$  W (pumps) and  $P_x = 0.1$  mW (signal). When the frequency difference  $\omega_d = 1.0$  Tr/s, dispersion cancels CPM exactly and the growth rate  $-k_i = 2\gamma_s P$  is maximal. The inverse MI produces 20 dB of signal gain in a distance of 0.46 Km. When  $\omega_d = 1.42$ , dispersion is stronger than CPM, but the signal still grows exponentially, with growth rate  $3^{1/2}\gamma_s P$ . Although the gain is reduced, the inverse MI still produces 18 dB of gain in 0.46 Km. When  $\omega_d = 1.73$ , the total mismatch  $\delta = 2\gamma_s P$ : The signal power increases quadratically with distance, rather than exponentially. In this case, the gain is reduced significantly, to only 13 dB. However, by increasing the distance to 0.99 Km, one can restore the gain to 20 dB (not shown). For reference,  $\omega_d = 1$  Tr/s corresponds to  $f_d = 159$  GHz, which is comparable to the channel spacings of 40-Gb/s

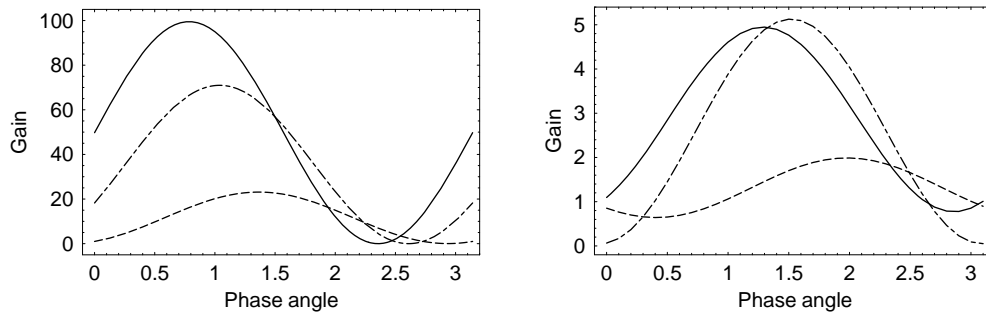


Fig. 12. Signal gain plotted as a function of the signal phase, for the fiber length  $l = 0.46$  Km, the pump powers  $P_1 = P_3 = 0.25$  W and the signal power  $P_2 = 0.1$  mW. The solid, dot-dashed and dashed curves represent frequency differences of 0.16, 0.23 and 0.28 THz, respectively. (a) Theoretical predictions based on Eq. (40). (b) Simulation results based on Eq. (1).

communication systems (100 and 200 GHz).

To test these theoretical predictions, we made scalar simulations based on Eq. (1), for the aforementioned parameters and the signal power  $P_2(0) = 0.1$  mW. When a frequency filter was used to restrict the simulations to three modes, the results obtained (not shown) agreed with the theoretical predictions. The simulation results obtained without a filter are shown in Fig. 12(b). In all three cases, the simulated gain depends periodically on the input phase, in qualitative agreement with the theoretical predictions. However, the simulated gain levels are much lower than their theoretical counterparts.

FWM cascades associated with the inverse MI are shown in Fig. 13, for cases in which  $\omega_d = 1$  Tr/s. (The other parameters are the same as those of Fig. 12.) For the signal phase  $\phi_2(0) = 0$ , the signal experiences little gain, whereas for  $\phi_2 = 1.3$ , the signal experiences some gain (7 dB). These results are consistent with Fig. 12(b). However, in both cases there are significant secondary pumps (odd harmonics) and secondary signals, or idlers (even harmonics). The presence of these harmonics affects the signal evolution significantly, as shown in Fig. 12.

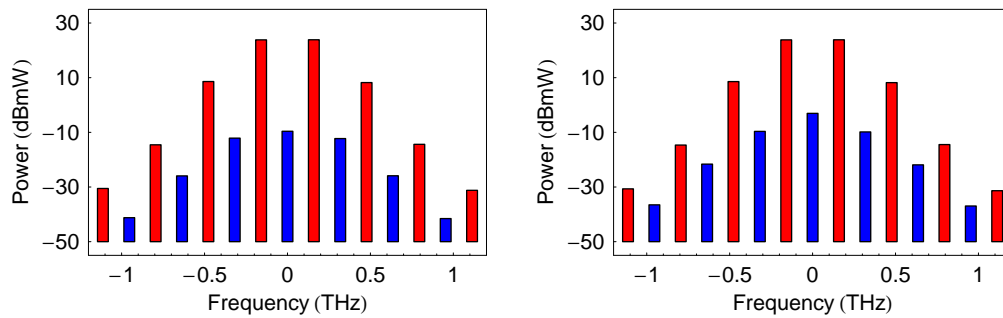


Fig. 13. Simulated mode power [Eq. (1)] plotted as a function of mode frequency, for the parameters of Fig. 12 and a frequency difference of 0.16 THz. (a) When the signal phase  $\phi_2 = 0$ , the signal experiences little gain. (b) When  $\phi_2 = 1.3$ , the signal experiences some gain. Red bars denote odd harmonics (pumps), whereas blue bars denote even harmonics (signal and idlers).

It is well known that FWM is driven by nonlinearity and suppressed by dispersion ( $\beta_2 \omega_d^2 / 2$ ). Hence, the powers of the pump harmonics should depend inversely on the frequency difference (channel spacing). In Fig. 14, the power of the first pump harmonic (which has a frequency of 0.48 THz) is plotted as a function of distance, for three different channel spacings. In each

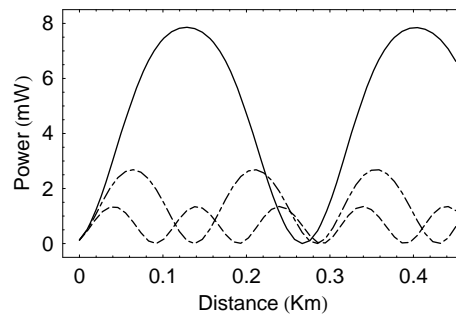


Fig. 14. Simulated power [Eq. (1)] of a secondary pump plotted as a function of distance, for the parameters of Fig. 12. The solid, dot-dashed and dashed curves represent frequency differences of 0.16, 0.23 and 0.28 THz, respectively.

case, the harmonic power is an oscillatory function of distance, so the measured power depends sensitively on the point at which it is measured. However, the peak power decreases as the channel spacing increases, as predicted.

The preceding results show that the potential signal gain is highest for a channel spacing of 1 Tr/s, but so also are the powers of the pump and signal harmonics. One can reduce the harmonic powers significantly by increasing the channel spacing to 1.73 Tr/s, but the benefits of weaker harmonics are offset by the significant reduction in gain. The best performance was obtained for the intermediate spacing of 1.42 Tr/s, for which moderate harmonic generation is accompanied by moderate gain. Consequently, we made additional simulations for this channel spacing, to determine how the gain depends on length. In Fig. 15, the signal gain is plotted as a function of the signal phase, for the fiber lengths  $l = 0.2, 0.4, 0.6$  and  $0.8$  Km. (The other parameters are the same as those of Fig. 4.) As the length increases, the gain increases, remains constant and decreases. The maximal gain of about 7 dB is attained for a length of about 0.5 Km [Figs. 12(b) and 13].

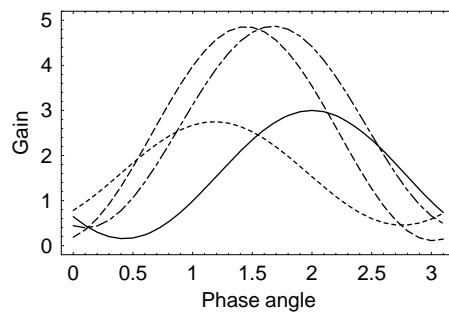


Fig. 15. Simulated signal gain [Eq. (1)] plotted as a function of signal phase, for the parameters of Fig. 12 and a frequency difference of 0.23 THz. The dotted, dashed, dot-dashed and solid curves represent lengths of 0.2, 0.4, 0.6 and 0.8 Km, respectively.

FWM cascades associated with the inverse MI are shown in Fig. 16, for cases in which  $\omega_d = 1.42$  Tr/s. (The other parameters are the same as those for Fig. 12.) Figures 16(a)–16(d) correspond to the lengths  $l = 0.2, 0.4, 0.6$  and  $0.8$ , and the signal phases  $\phi_2 = 1.2, 1.4, 1.7$  and  $2.0$  (maximal growth), respectively. In all cases, the secondary pumps are weaker than the primary pumps, and the idlers are weaker than the signal. (The secondary pump powers vary with distance, as shown in Fig. 13.) Nonetheless, the presence of weak FWM products is enough to limit the signal gain to about 7 dB. Further study of this frequency configuration (in which all frequencies are far from the ZDF) is required.

#### 4.2. Phase-insensitive amplification and frequency conversion

Although the focus of this report was the inverse MI, which provides phase-sensitive amplification, the discussion of parametric interactions in Sec. 3 included PC [Eqs. (41) and (42)] and BS [Eqs. (43) and (44)]. PC provides phase-insensitive amplification, whereas BS provides phase-insensitive frequency conversion (provided that there are no input idlers). It was shown in [26] that strong birefringence suppresses vector PC, which involves  $x$ - and  $y$ -polarized pumps, and  $x$ - and  $y$ -polarized sidebands. This result, which was explained in Sec. 3, implies that scalar  $x$ -polarized PC and  $y$ -polarized PC are independent processes. It was stated in [25] that birefringence inhibits vector BS, which involves  $x$ -polarized pumps and  $y$ -polarized sidebands, or  $x$ - and  $y$ -polarized pumps, and  $x$ - and  $y$ -polarized sidebands [6]. This statement, which was also explained in the Sec. 3, implies that scalar  $x$ -polarized BS and  $y$ -polarized BS are independent

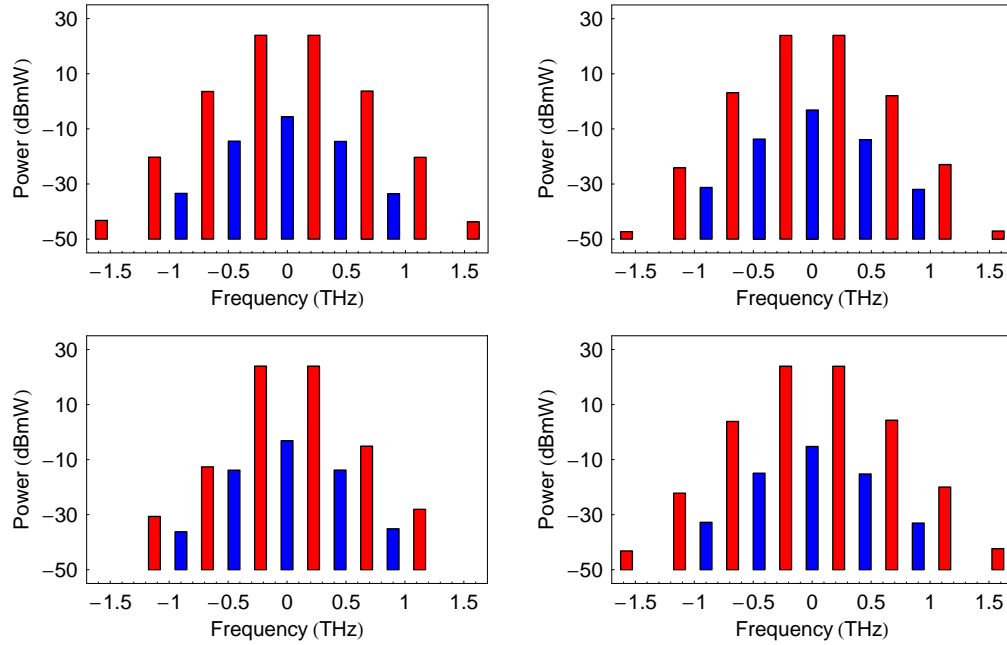


Fig. 16. Simulated mode power [Eq. (1)] plotted as a function of mode frequency, for the parameters of Fig. 12 and a frequency difference of 0.23 THz. Figures 16(a)–16(d) correspond to lengths of 0.2, 0.4, 0.6 and 0.8, respectively. Red bars denote odd harmonics (pumps), whereas blue bars denote even harmonics (signal and idlers).

processes.

Equations (38) and (41) were used to model PC for the fiber parameters  $\beta_3 = 0.03 \text{ ps}^3/\text{Km}$ ,  $\beta_4 = -3 \times 10^{-4} \text{ ps}^4/\text{Km}$ ,  $\gamma = 10/\text{Km-W}$  and  $l = 1.0 \text{ Km}$ , and the pump powers  $P_2 = P_3 = 0.25 \text{ W}$ . (The slowness parameter  $\beta_1$  has no effect on PC when the waves are co-polarized.) The dependence of the signal gain  $P_1(z)/P_1(0)$  on the pump and signal frequencies was studied [17]. In Fig. 17, the gain is plotted as a function of the signal frequency, for the pump frequencies  $\omega_2 = -21.1$  and  $\omega_3 = 22.9 \text{ Tr/s}$  (measured relative to the ZDF). For reference,  $\beta_2(\omega_a) = 0.028$ , where  $\omega_a = (\omega_2 + \omega_3)/2$  is the average of the pump frequencies. The PC equations predict that

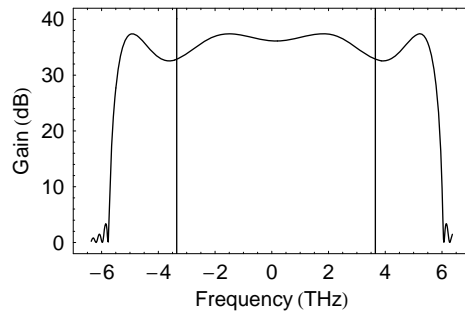


Fig. 17. Signal gain [Eqs. (38) and (41)] plotted as a function of signal frequency, for a fiber length of 1.0 Km. The pump frequencies are  $-3.35$  and  $3.65 \text{ THz}$  (solid lines), and the (common) pump power is  $0.25 \text{ W}$ .

signals with a wide range of frequencies will be amplified by about 36 dB. Outer gain bands ( $\omega_1 < \omega_2 < \omega_3 < \omega_4$ ) and inner bands ( $\omega_2 < \omega_1 < \omega_4 < \omega_3$ ) exist simultaneously because  $\beta_4 < 0$  [24].

To test the theoretical predictions, we made scalar and vector simulations based on the Eqs. (1) and (2), for the aforementioned fiber parameters (in addition to which  $\beta_{1x} = 50$  and  $\beta_{1y} = -50$  ps/Km) and pump frequencies. In the first two simulations, the pumps were either  $x$ -polarized ( $P_{2x} = P_{3x} = 0.25$  and  $P_{2y} = P_{3y} = 0.0$  W) or  $y$ -polarized ( $P_{2x} = P_{3x} = 0.0$  and  $P_{2y} = P_{3y} = 0.25$  W) and  $x$ - or  $y$ -polarized noise sources (with powers of  $10^{-5}$  mW per frequency bin) were used to seed PC. The spectra are shown in Fig. 18. Their main features (gain levels and locations of the gain maxima) are consistent with the theoretical predictions. For frequencies that are comparable to the pump frequencies, the predicted gains are higher than the simulated gains, because the PC equations omit the effects of sidebands produced by simultaneous MI and BS [17].

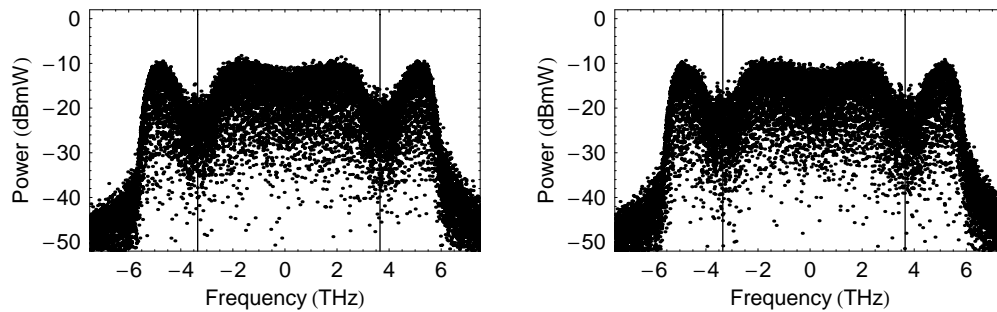


Fig. 18. Simulated sideband power [Eqs. (1) and (2)] plotted as a function of frequency. The pump frequencies are  $-3.35$  and  $3.65$  THz (solid lines), the (common) pump power is  $0.25$  W and the noise power is  $-50$  dBmW. (a) Pumps and sidebands are  $x$ -polarized. (b) Pumps and sidebands are  $y$ -polarized.

In the third simulation both pumps were polarized at  $45^\circ$  to the fiber axes ( $P_{2x} = P_{2y} = 0.25$  and  $P_{3x} = P_{3y} = 0.25$  W). The spectra, which are shown in Fig. 19, are almost identical to the spectra of Fig. 18. (Differences exist between the simulated gains for individual frequencies, because different noise seeds were used.) This result confirms that polarization-independent (phase-insensitive) amplification is possible in a SBF, for a wide range of signal frequencies.

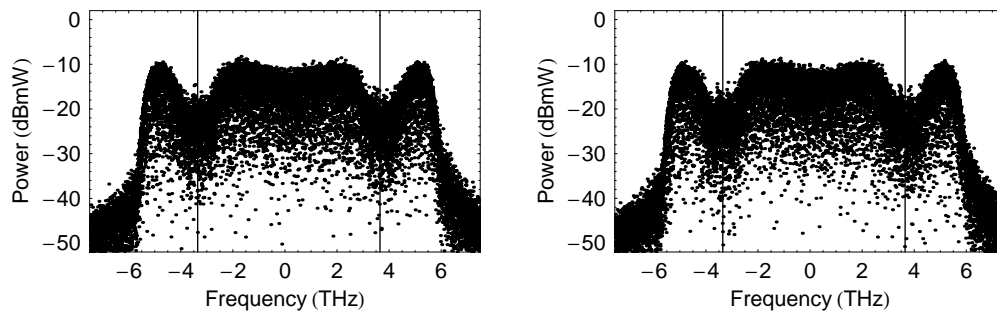


Fig. 19. Simulated sideband power [Eqs. (1) and (2)] plotted as a function of frequency. The pump frequencies are  $-3.35$  and  $3.65$  THz (solid lines), the (common) pump power is  $0.25$  W in each polarization and the noise power is  $-50$  dBmW in each polarization. (a)  $x$ -polarized power. (b)  $y$ -polarized power.

Equations (39) and (44) were used to model BS for the fiber parameters  $\beta_3 = 0.03 \text{ ps}^3/\text{Km}$ ,  $\beta_4 = -3 \times 10^{-4} \text{ ps}^4/\text{Km}$ ,  $\gamma = 10/\text{Km}\cdot\text{W}$  and  $l = 0.31 \text{ Km}$ , and the pump powers  $P_1 = P_3 = 0.25 \text{ W}$ . ( $\beta_1$  has no effect on BS when the waves are co-polarized.) The dependence of the signal-to-idler conversion efficiency  $P_4(z)/P_2(0)$  on the pump and signal frequencies was studied [25]. In Fig. 20, the conversion efficiency is plotted as a function of the lower pump frequency  $\omega_1$ , for the signal frequency  $\omega_2 = -9.26 \text{ Tr/s}$  and higher pump frequency  $\omega_3 = 10.74 \text{ Tr/s}$  (measured relative to the ZDF). For reference,  $\beta_2(\omega_a) = 0.022$ , where  $\omega_a = (\omega_2 + \omega_3)/2$  is the average of the signal frequency and the higher pump frequency. The BS equations predict that the conversion efficiency will be higher than  $-1 \text{ dB}$  for a wide range of lower pump and idler frequencies (so the idler frequency can be tuned). The hollow circles denote lower pump and idler frequencies of  $-19.26$  and  $20.74 \text{ Tr/s}$ , respectively, for which the predicted conversion efficiency is  $-0.36 \text{ dB}$ , whereas the solid circles denote frequencies of  $-29.26$  and  $30.74 \text{ Tr/s}$ , for which the conversion efficiency is  $-0.25 \text{ dB}$ .

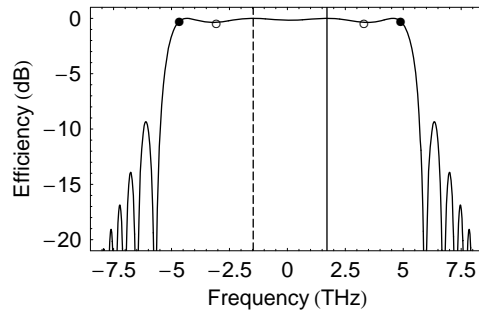


Fig. 20. Signal-to-idler conversion efficiency [Eqs. (39) and (44)] plotted as a function of the lower pump frequency, for a fiber length of 0.31 Km. The signal frequency is  $-1.47 \text{ THz}$  (dashed line), the higher pump frequency is  $1.71 \text{ THz}$  (solid line) and the (common) pump power is  $0.25 \text{ W}$ . The hollow circles denote lower pump and idler frequencies of  $-3.07$  and  $3.3 \text{ THz}$ , respectively, whereas the solid circles denote frequencies of  $-4.66$  and  $4.89 \text{ THz}$ .

To test the theoretical predictions, we made scalar and vector simulations based on Eqs. (1) and (2), for the aforementioned fiber parameters (in addition to which  $\beta_{1x} = 50$  and  $\beta_{1y} = -50 \text{ ps/Km}$ ), and pump and signal frequencies. The spectra shown in Fig. 21 were obtained for  $x$ -

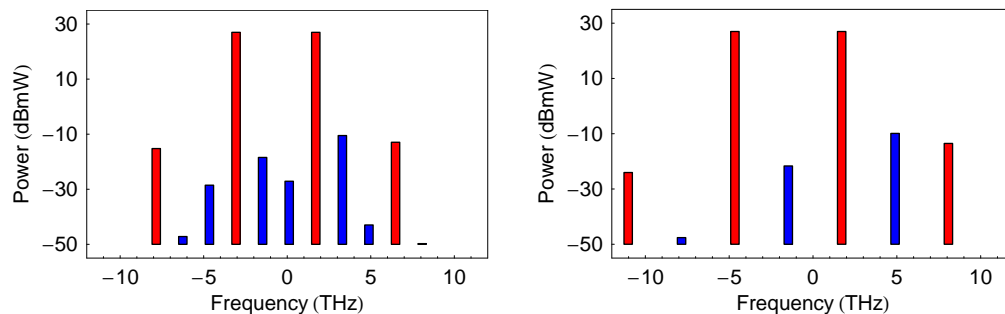


Fig. 21. Simulated mode power [Eq. (1)] plotted as a function of mode frequency. The signal frequency is  $-1.47 \text{ THz}$ , the higher pump frequency is  $1.71 \text{ THz}$  and the (common) pump power is  $0.25 \text{ W}$ . (a) The lower pump (idler) frequency is  $-3.07$  ( $3.30$ )  $\text{THz}$ . (b) The lower pump (idler) frequency is  $-4.66$  ( $4.89$ )  $\text{THz}$ . Red bars denote pumps, whereas blue bars denote signal and idlers.

polarized pumps and sidebands ( $P_{1x} = P_{3x} = 0.25$  and  $P_{1y} = P_{3y} = 0.0$  W). For the lower pump frequency  $\omega_1 = -19.26$  Tr/s and the idler frequency  $\omega_4 = 10.74$  Tr/s, a conversion efficiency of  $-0.50$  dB was obtained [Fig. 21(a)]. This conversion efficiency is 0.14 dB lower than the predicted value, because of weak coupling to secondary modes. The figure shows two (pump) modes produced by pump–pump FWM, and two (idler) modes produced by MI and PC. For the frequencies  $\omega_1 = -29.26$  Tr/s and  $\omega_4 = 20.74$  Tr/s, a conversion efficiency of 0.11 dB was obtained [Fig. 21(b)]. This conversion efficiency is 0.36 dB higher than predicted, because of weak (phase-sensitive) coupling to secondary modes. The figure shows two (pump) modes produced by pump–pump FWM. In both cases, the signal is attenuated by about 10 dB, so the corrections to the conversion efficiency are relatively small. Larger frequency differences between the lower pump and signal, and the higher pump (stronger dispersion), correspond(s) to weaker secondary modes.

In Fig. 22, the conversion efficiency is plotted as a function of the signal polarization for pumps polarized at  $45^\circ$  to the fiber axes ( $P_{1x} = P_{1y} = 0.25$  and  $P_{3x} = P_{3y} = 0.25$  W). For both idler frequencies (3.30 and 4.89 THz), the polarization dependence of the conversion efficiency is very weak ( $\leq 0.01$  dB). These results confirm that polarization-independent frequency conversion is possible in a SBF, for a wide range of idler frequencies.

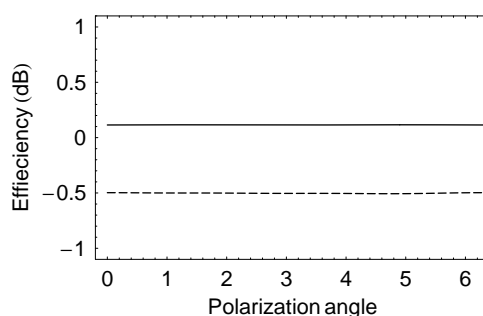


Fig. 22. Simulated conversion efficiency [Eqs. (1) and (2)] plotted as a function of signal polarization. The signal frequency is  $-1.47$  THz, the higher pump frequency is  $1.71$  THz and the (common) pump power is  $0.25$  W in each polarization. The dashed curve represents a lower pump (idler) frequency of  $-3.07$  ( $3.30$ ) THz, whereas the solid curve represents a lower pump (idler) frequency of  $-4.66$  ( $4.89$ ) THz.

The preceding results were based on the assumption that the second- and higher-order dispersion coefficients are the same for both axes. However, the ZDFs of some fibers differ by amounts of order 1 Tr/s. Such differences reduce the bandwidths over which amplification and frequency conversion are polarization independent (because the gain and conversion curves are offset in frequency). ZDF variations decrease the gain levels and conversion efficiencies [21], but should not affect the polarization dependence of PC and BS (unless the ZDFs vary independently).

## 5. Summary

The inverse modulation interaction (MI) is a degenerate four-wave mixing process in which two strong pumps drive a weak signal, whose frequency is the average of the pump frequencies. In this report, detailed studies were made of the phase and polarization dependence of the inverse MI in a strongly-birefringent fiber. In the first study (Sec. 3.2), all of the wave frequencies were comparable to the zero-dispersion frequency (ZDF) of the fiber, so the effects of dispersion were unimportant. For parameters that are typical of current experiments,

birefringence decouples the evolution of the  $x$  and  $y$  components of the waves, where  $x$  and  $y$  denote the birefringence axes. Hence, if two pumps are linearly polarized at  $45^\circ$  to these axes, the phase-sensitive amplification (and attenuation) experienced by a linearly-polarized signal is independent of its polarization angle. This behavior was explained theoretically, in terms of the walk-off between time-dependent contributions to different components [Eqs. (7) and (8)], and verified numerically, by simulations based on the coupled Schrödinger equations [Eqs. (1) and (2)]. However, because dispersion is weak near the ZDF, secondary FWM processes produce a cascade of weak secondary pumps and signals (idlers), which consumes bandwidth and depletes the pumps.

In the second study (Sec. 4.1), most of the wave frequencies were far from the ZDF, so the effects of dispersion were important. For parameters that are typical of current experiments, dispersion reduces, but does not eliminate completely, the cascade of secondary waves produced by other FWM processes. Two alternative configurations were considered. In the first configuration, the pump frequencies were far from the ZDF, but the signal frequency was near the ZDF. The presence of a weak cascade did not affect the signal evolution significantly. If the pumps are linearly polarized at  $45^\circ$  to the birefringence axes, the signal still experiences polarization-independent phase-sensitive amplification. In the second configuration, the pump and signal frequencies were all far from the ZDF, but close to each other. Although the signal evolved in a phase-sensitive manner, the presence of a moderate cascade limited the signal amplification significantly.

This report focused on the inverse MI, in which two strong pumps drive one weak signal. However, similar results are obtained for a variant of the MI, in which one strong pump drives a pair of signals, whose frequencies are equally spaced about the pump frequency [27, 28]: If the pump is linearly polarized at  $45^\circ$  to the birefringence axes, a linearly-polarized signal pair experiences phase-sensitive amplification and attenuation that is independent of their (common) polarization angle.

Studies were also made of nondegenerate FWM processes in which two strong pumps drive weak (signal and idler) sidebands (Sec. 4.2). In phase conjugation (PC), the sum of the sideband frequencies equals the sum of the pump frequencies, whereas in Bragg scattering (BS), the difference between the sideband frequencies equals the difference between the pump frequencies. PC provides phase-insensitive amplification, whereas BS provides phase-insensitive frequency conversion. Dispersion affects both processes. If the pumps are polarized at  $45^\circ$  to the birefringence axes, signals experience polarization-independent amplification and frequency conversion. The weak cascades that occur do not degrade significantly the properties of PC and BS. However, the bandwidths of these polarization-independent processes are limited by the small difference between the zero-dispersion frequencies of the two axes.

## Appendix: Power conservation by distant-wave interactions

The interaction of waves 1–4 is governed by CMEs (30) and (31) for  $X_1$  and  $X_2$ , respectively, and their analogs for  $X_3$ ,  $X_4$  and  $Y_1$ – $Y_4$ . The purpose of this appendix is to show that these CMEs conserve the total powers of the  $x$ - and  $y$ -components ( $P_x$  and  $P_y$ ). Linear wavenumber shifting (caused by dispersion) and nonlinear wavenumber shifting (caused by SPM and CPM) do not change the powers of the  $x$ - and  $y$ -components of waves 1–4 ( $P_{jx}$  and  $P_{jy}$ ), so these processes need not be considered explicitly.

First, consider the scalar FWM processes in which  $2\pi_{2x} \leftrightarrow \pi_{3x} + \pi_{1x}$ ,  $\pi_{2x} + \pi_{3x} \leftrightarrow \pi_{4x} + \pi_{1x}$  and  $2\pi_{3x} \leftrightarrow \pi_{4x} + \pi_{2x}$ . The first and third processes are degenerate, whereas the second is nondegenerate. By combining the associated terms in the CMEs, one finds that

$$d_z |X_1|^2 = i\gamma_s X_1^* X_2^2 X_3^* + i2\gamma_s X_1^* X_2 X_3 X_4^* + \text{c.c.}, \quad (45)$$

$$d_z|X_2|^2 = i2\gamma_s X_1 (X_2^*)^2 X_3 + i2\gamma_s X_1 X_2^* X_3^* X_4 + i\gamma_s X_2^* X_3^2 X_4^* + \text{c.c.}, \quad (46)$$

$$d_z|X_3|^2 = i\gamma_s X_1^* X_2^2 X_3^* + i2\gamma_s X_1 X_2^* X_3^* X_4 + i2\gamma_s X_2 (X_3^*)^2 X_4 + \text{c.c.}, \quad (47)$$

$$d_z|X_4|^2 = i2\gamma_s X_1^* X_2 X_3 X_4^* + i\gamma_s X_2^* X_3^2 X_4^* + \text{c.c.} \quad (48)$$

Equations (45)–(48) imply that

$$d_z(P_{1x} + P_{2x} + P_{3x} + P_{4x}) = 0. \quad (49)$$

Although scalar FWM allows the  $x$ -components to exchange power, it conserves their total power. The properties of scalar FWM among the  $y$ -components are similar.

Second, consider the CPR process in which  $\pi_{1x} + \pi_{2y} \leftrightarrow \pi_{1y} + \pi_{2x}$ . By combining the associated terms in the CMEs, one finds that

$$d_z|X_1|^2 = i\gamma_c X_1^* Y_1 X_2 Y_2^* + \text{c.c.}, \quad (50)$$

$$d_z|Y_1|^2 = i\gamma_c X_1 Y_1^* X_2^* Y_2 + \text{c.c.}, \quad (51)$$

$$d_z|X_2|^2 = i\gamma_c X_1 Y_1^* X_2^* Y_2 + \text{c.c.}, \quad (52)$$

$$d_z|Y_2|^2 = i\gamma_c X_1^* Y_1 X_2 Y_2^* + \text{c.c.} \quad (53)$$

Equations (50)–(53) imply that

$$d_z(P_{1x} + P_{2x}) = 0 = d_z(P_{1y} + P_{2y}), \quad (54)$$

$$d_z(P_{1x} + P_{1y}) = 0 = d_z(P_{2x} + P_{2y}). \quad (55)$$

Not only does CPR conserve the total powers of the  $x$ - and  $y$ -components, it also conserves the total powers of waves 1 and 2. The properties of the other five CPR processes, in which  $\pi_{jx} + \pi_{ky} \leftrightarrow \pi_{jy} + \pi_{kx}$ , are similar.

Third, consider the CPM instability in which  $\pi_{2x} + \pi_{2y} \leftrightarrow \pi_{3y} + \pi_{1x}$ . This FWM process is frequency degenerate, but polarization nondegenerate. By combining the associated terms in the CMEs, one finds that

$$d_z|X_1|^2 = i\gamma_c X_1^* X_2 Y_2 Y_3^* + \text{c.c.}, \quad (56)$$

$$d_z|X_2|^2 = i\gamma_c X_1 X_2^* Y_2^* Y_3 + \text{c.c.}, \quad (57)$$

$$d_z|Y_2|^2 = i\gamma_c X_1 X_2^* Y_2^* Y_3 + \text{c.c.}, \quad (58)$$

$$d_z|Y_3|^2 = i\gamma_c X_1^* X_2 Y_2 Y_3^* + \text{c.c.} \quad (59)$$

Equations (56)–(59) imply that

$$d_z(P_{1x} + P_{2x}) = 0 = d_z(P_{2y} + P_{3y}). \quad (60)$$

Because one  $x$ -component is a pump and the other is a sideband, and one  $y$ -component is a pump and the other is a sideband, the total powers of the  $x$ - and  $y$ -components are conserved. The properties of the other CPM instabilities, in which  $\pi_{2x} + \pi_{2y} \leftrightarrow \pi_{3x} + \pi_{1y}$ ,  $\pi_{3x} + \pi_{3y} \leftrightarrow \pi_{4y} + \pi_{2x}$  and  $\pi_{3x} + \pi_{3y} \leftrightarrow \pi_{4x} + \pi_{2y}$ , are similar.

Fourth, consider the vector FWM process in which  $\pi_{2y} + \pi_{3x} \leftrightarrow \pi_{4y} + \pi_{1x}$ . This process is frequency and polarization nondegenerate. By combining the associated terms in the CMEs, one finds that

$$d_z|X_1|^2 = i\gamma_c X_1^* Y_2 X_3 Y_4^* + \text{c.c.}, \quad (61)$$

$$d_z|Y_2|^2 = i\gamma_c X_1 Y_2^* X_3^* Y_4 + \text{c.c.}, \quad (62)$$

$$d_z|X_3|^2 = i\gamma_c X_1 Y_2^* X_3^* Y_4 + \text{c.c.}, \quad (63)$$

$$d_z|Y_4|^2 = i\gamma_c X_1^* Y_2 X_3 Y_4^* + \text{c.c.} \quad (64)$$

Equations (61)–(64) imply that

$$d_z(P_{1x} + P_{3x}) = 0 = d_z(P_{2y} + P_{4y}). \quad (65)$$

Because one  $x$ -component is a pump and the other is a sideband, and one  $y$ -component is a pump and the other is a sideband, the total powers of the  $x$ - and  $y$ -components are conserved. The properties of the other vector FWM processes, in which  $\pi_{2y} + \pi_{3x} \leftrightarrow \pi_{4x} + \pi_{1y}$ ,  $\pi_{2x} + \pi_{3y} \leftrightarrow \pi_{4y} + \pi_{1x}$  and  $\pi_{2x} + \pi_{3y} \leftrightarrow \pi_{4x} + \pi_{1y}$ , are similar. Thus, all the processes in which the waves participate conserve the total powers of the  $x$ - and  $y$ -components, as stated in Sec. 3.